
This is an electronic reprint of the original article.
This reprint may differ from the original in pagination and typographic detail.

Tiitinen, Lauri; Hinkkanen, Marko; Harnefors, Lennart

Design Framework for Sensorless Control of Synchronous Machine Drives

Published in:
IEEE Transactions on Industrial Electronics

DOI:
[10.1109/TIE.2024.3429650](https://doi.org/10.1109/TIE.2024.3429650)

Published: 01/01/2025

Document Version
Publisher's PDF, also known as Version of record

Published under the following license:
CC BY

Please cite the original version:
Tiitinen, L., Hinkkanen, M., & Harnefors, L. (2025). Design Framework for Sensorless Control of Synchronous Machine Drives. *IEEE Transactions on Industrial Electronics*, 72(2), 1379-1390. Article 10621712. <https://doi.org/10.1109/TIE.2024.3429650>

This material is protected by copyright and other intellectual property rights, and duplication or sale of all or part of any of the repository collections is not permitted, except that material may be duplicated by you for your research use or educational purposes in electronic or print form. You must obtain permission for any other use. Electronic or print copies may not be offered, whether for sale or otherwise to anyone who is not an authorised user.

Design Framework for Sensorless Control of Synchronous Machine Drives

Lauri Tiitinen , Marko Hinkkanen , *Fellow, IEEE*, and Lennart Harnefors , *Fellow, IEEE*

Abstract—This article develops a design framework for sensorless flux-vector control of synchronous machine drives. Observer-based volts-per-hertz (V/Hz) control is presented as a special case in this framework. A complete linearized model is derived, which allows systematic control design and stability analysis. Using the model, passivity conditions are derived. The control methods are experimentally evaluated using a 6.7-kW synchronous reluctance machine (SyRM) and a 2.2-kW permanent-magnet (PM) machine as examples.

Index Terms—Flux-vector control, passivity, permanent-magnet synchronous machines (PMSMs), sensorless, stability, synchronous reluctance machines (SyRMs), volts-per-hertz (V/Hz) control.

I. INTRODUCTION

SYNCHRONOUS machines, including permanent-magnet (PM) and synchronous reluctance machines (SyRMs), are increasing their share in industrial drives. For these machines, current-based vector control schemes have been conventionally used [1], [2], [3], [4]. In saturable machines, the closed-loop current control becomes nonlinear, which has been considered in more recent works on current-vector control [5], [6].

Flux-vector control [7], [8], [9], [10], [11] has some advantages over current-vector control. Since the stator-flux magnitude and the electromagnetic torque (or torque-producing current) are used as the control variables, the computation of optimal control trajectories and the implementation of field-weakening operation becomes simpler. In some related schemes, the load angle is used as the control variable instead of the torque [12]. Direct torque control (DTC) is another related

Manuscript received 10 January 2024; revised 23 January 2024, 21 April 2024, 27 May 2024, and 30 June 2024; accepted 4 July 2024. This work was supported in part by ABB Oy and in part by the Research Council of Finland Centre of Excellence in High-Speed Electromechanical Energy Conversion Systems. (Corresponding author: Lauri Tiitinen.)

Lauri Tiitinen and Marko Hinkkanen are with the Department of Electrical Engineering and Automation, Aalto University, 02150 Espoo, Finland (e-mail: lauri.tiitinen@aalto.fi; marko.hinkkanen@aalto.fi).

Lennart Harnefors is with ABB Corporate Research, 72226 Västerås, Sweden (e-mail: lennart.harnefors@se.abb.com).

Color versions of one or more figures in this article are available at <https://doi.org/10.1109/TIE.2024.3429650>.

Digital Object Identifier 10.1109/TIE.2024.3429650

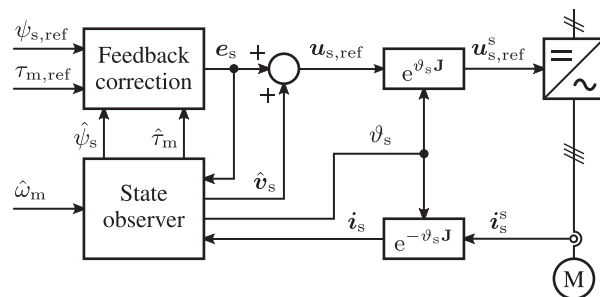


Fig. 1. Flux-vector control consisting of a state observer and state feedback $u_{s,\text{ref}} = \hat{v}_s + e_s$, where the term $\hat{v}_s = R_s i_s + \hat{\omega}_m J \hat{\psi}_s$ is for feedback linearization and e_s is the control error term. The inputs to the controller are the flux magnitude reference $\psi_{s,\text{ref}}$ and the reference for the electromagnetic torque $\tau_{m,\text{ref}}$.

control scheme [13], [14]. However, its conventional hysteresis-control based implementations introduce unpredictable switching frequency and torque ripple [15].

In flux-vector control, proportional–integral (PI) controllers are conventionally used for the two control variables. However, the flux-vector torque-control loop is nonlinear, even if magnetic saturation effects are not considered. Tuning can be difficult, as control performance depends on the operating point [16]. Therefore, the torque-control dynamics are typically only designed for a single operating point.

A nonlinear controlled system can be linearized as seen by the controller by means of feedback linearization [17]. Consequently, the two control channels can be decoupled, and the desired bandwidth is achieved for both control variables in all operating points [16]. In [18], this exact input-output feedback linearization method is extended with consideration for magnetic saturation.

Fig. 1 depicts the core of flux-vector control considered in this article. Fig. 2(a) shows its speed-controlled configuration, where the measured rotor speed is fed back to the control system. In many industrial applications, however, speed measurement is not feasible. Fig. 2(b) shows a speed-sensorless version of flux-vector control.

In addition to vector control modes, industrial drives typically incorporate a volts-per-hertz (V/Hz) control mode. Due to its simplicity, V/Hz control has remained popular in many applications, such as fans, pumps, and compressors, where precise torque control is not required. V/Hz control of synchronous machines is inherently unstable without additional compensators. Conventionally, compensation loops based on stator current

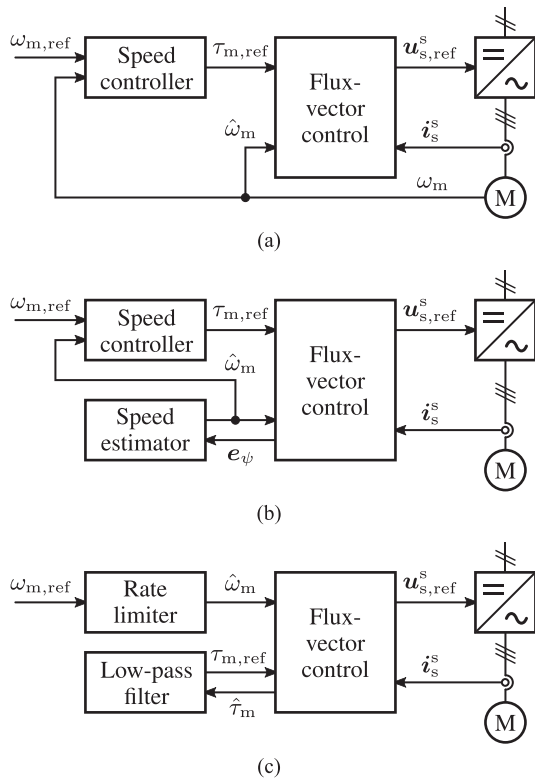


Fig. 2. Flux-vector control: (a) sensed; (b) sensorless; and (c) configured as V/Hz control. (a) Signal $\hat{\omega}_m = \omega_m$ is the measured speed. Flux-vector control core is the same in all configurations.

perturbations are used for this purpose [19], [20], [21]. However, analytical stability results and general design rules for a wide range of machines are not available for the compensation-loop based methods. In contrast, observer-based V/Hz control uses a passivity-based design, incorporating a sensorless flux observer and a state-feedback law to achieve stability in the whole feasible operating region [22].

This article presents a systematic design and analysis framework for flux-vector control of synchronous machines. The unified control framework can be configured for a wide range of drive systems: the flux-vector control mode can be used for applications with high-performance control requirements, while V/Hz configuration can be used for simpler applications such as fans and pumps. The main focus of the article is in sensorless configurations, while the speed-sensored variant is presented for comparison. First, in Section II, a synchronous machine model is presented. The main contributions of the article are presented as follows.

- 1) Based on the flux-magnitude and torque dynamics, flux-vector control is derived in Section III. The presented method can be seen as a generalized version of [16].
- 2) The observer-based V/Hz control, illustrated in Fig. 2(c), is shown as a special case of flux-vector control, where neither speed controller nor speed estimator is needed. Compared to conventional V/Hz control methods, the observer-based V/Hz control is passive (and stable) in any feasible operating point for all synchronous machines, and the tuning of its design is based on physical parameters.

- 3) A linearized model for the whole sensorless flux-vector control system, without simplifying assumptions in the torque-production or speed-estimation dynamics, is presented in Section IV. Furthermore, based on the linearized model, the passivity conditions for flux-vector control are derived and discussed. The derived analytical results hold valid for all synchronous machine types. The analysis shows that the sensorless drive system is locally stable at all operating points in the full speed and load range. At zero frequency, the system is marginally stable.

Section V considers implementation of the control method. Section VI shows experimental results, where a 6.7-kW four-pole SyRM and a 2.2-kW six-pole interior PM machine are used as examples. Finally, Section VII concludes the article.

II. SYSTEM MODEL

Space vectors are represented using column vectors. Per-unit (p.u.) quantities will be assumed.

A. State Equations

The machine is modeled in general coordinates, whose angular position is ϑ_s and the angular speed is $\omega_s = d\vartheta_s/dt$, both with respect to the stator. The electrical angular position and speed of the rotor d-axis are denoted by ϑ_m and $\omega_m = d\vartheta_m/dt$, respectively. The stator inductance matrix and the PM flux linkage vector, respectively, are

$$\mathbf{L}_s(\delta) = e^{\delta\mathbf{J}} \begin{bmatrix} L_d & 0 \\ 0 & L_q \end{bmatrix} e^{-\delta\mathbf{J}} \quad \boldsymbol{\psi}_f(\delta) = e^{\delta\mathbf{J}} \begin{bmatrix} \psi_f \\ 0 \end{bmatrix} \quad (1)$$

where L_d is the direct-axis inductance, L_q is the quadrature-axis inductance, ψ_f is the PM flux linkage, $\delta = \vartheta_m - \vartheta_s$ is the angle of the rotor d-axis with respect to the coordinate system, and $\mathbf{J} = \begin{bmatrix} 0 & -1 \\ 1 & 0 \end{bmatrix}$ is the orthogonal rotation matrix.

The state equations are

$$\frac{d\boldsymbol{\psi}_s}{dt} = \mathbf{u}_s - R_s \mathbf{i}_s - \omega_s \mathbf{J} \boldsymbol{\psi}_s \quad (2a)$$

$$\frac{d\delta}{dt} = \omega_m - \omega_s \quad (2b)$$

where $\boldsymbol{\psi}_s$ is the stator flux linkage, \mathbf{u}_s is the stator voltage, and R_s is the stator resistance. The stator current and the electromagnetic torque, respectively, are nonlinear functions of the state variables

$$\mathbf{i}_s = \mathbf{L}_s^{-1}(\delta) [\boldsymbol{\psi}_s - \boldsymbol{\psi}_f(\delta)] \quad (2c)$$

$$\tau_m = (\mathbf{J}\boldsymbol{\psi}_s)^T \mathbf{i}_s. \quad (2d)$$

As special cases, this model represents a surface-mounted PM machine if $L_d = L_q$ and an SyRM if $\psi_f = 0$.

B. Flux-Magnitude and Torque Dynamics

The two controlled variables of the flux-vector control system are the stator-flux magnitude $\psi_s = \|\boldsymbol{\psi}_s\|$ and the electromagnetic torque τ_m . Therefore, to develop and analyze the control system, the flux-magnitude and torque dynamics are derived.

From (2a), the dynamics of the flux magnitude can be rewritten in the form

$$\frac{d\psi_s}{dt} = \frac{\psi_s^T}{\|\psi_s\|} (\mathbf{u}_s - R_s \mathbf{i}_s - \omega_m \mathbf{J} \psi_s). \quad (3a)$$

The last term of (3a) does not affect the dynamics since $\psi_s^T \mathbf{J} \psi_s = 0$.

The torque in (2d) can be expressed as a function of the stator flux ψ_s and the angle δ . The torque dynamics are

$$\begin{aligned} \frac{d\tau_m}{dt} &= \frac{\partial \tau_m(\psi_s, \delta)}{\partial \psi_s} \frac{d\psi_s}{dt} + \frac{\partial \tau_m(\psi_s, \delta)}{\partial \delta} \frac{d\delta}{dt} \\ &= (\mathbf{J} \mathbf{i}_a)^T \frac{d\psi_s}{dt} - \tau_\delta \frac{d\delta}{dt} \\ &= (\mathbf{J} \mathbf{i}_a)^T (\mathbf{u}_s - R_s \mathbf{i}_s - \omega_m \mathbf{J} \psi_s) \end{aligned} \quad (3b)$$

where the auxiliary current $\mathbf{i}_a = -\mathbf{J}(\partial \mathbf{i}_s / \partial \delta)$ is defined as¹

$$\mathbf{i}_a = \mathbf{L}_s^{-1}(\delta) \psi_f(\delta) - [\mathbf{L}_s^{-1}(\delta) + \mathbf{J} \mathbf{L}_s^{-1}(\delta) \mathbf{J}] \psi_s \quad (3c)$$

and the torque factor is

$$\tau_\delta = \mathbf{i}_a^T \psi_s. \quad (3d)$$

This torque factor can be interpreted as the electromagnetic torque per radian as the flux magnitude is kept constant. Furthermore, $\tau_\delta = 0$ is the maximum-torque-per-volt (MTPV) limit, and $\tau_\delta > 0$ holds in the feasible operating region as shown in Appendix A.

III. FLUX-VECTOR CONTROL

The block diagram of the flux-vector control system is shown in Fig. 1. It consists of a state observer and a state-feedback law, which can be reasoned based on the principle of feedback linearization [23]. The control law is valid in any coordinate system. For simplicity, the observer is described here in estimated rotor coordinates, corresponding to $\vartheta_s = \hat{\vartheta}_m$, since the inductance matrix estimate and the PM flux estimate are constant in these coordinates, i.e.,

$$\hat{\mathbf{L}}_s = \begin{bmatrix} L_d & 0 \\ 0 & L_q \end{bmatrix} \quad \hat{\psi}_f = \begin{bmatrix} \psi_f \\ 0 \end{bmatrix}. \quad (4)$$

Linear magnetics are considered in the model and the control law. If desired, these could be relatively easily extended with nonlinear magnetics [18].

A. Control Law

Based on the flux-magnitude and torque dynamics in (3), the voltage reference can be chosen as

$$\mathbf{u}_{s,\text{ref}} = R_s \mathbf{i}_s + \hat{\omega}_m \mathbf{J} \hat{\psi}_s + \mathbf{e}_s \quad (5a)$$

with the control error term

$$\mathbf{e}_s = \mathbf{k}_\psi (\psi_{s,\text{ref}} - \hat{\psi}_s) + \mathbf{k}_\tau (\tau_{m,\text{ref}} - \hat{\tau}_m) \quad (5b)$$

¹As a special case, the auxiliary current reduces to $\mathbf{i}_a = \psi_f(\delta)/L_d$ if $L_d = L_q$.

where $\psi_{s,\text{ref}}$ is the flux-magnitude reference and $\tau_{m,\text{ref}}$ is the torque reference. As shown in Appendix B, the flux and torque channels become decoupled, if the gain vectors are of the form

$$\mathbf{k}_\psi = k_\psi \frac{\hat{\mathbf{i}}_a}{\|\hat{\mathbf{i}}_a\|} \quad \mathbf{k}_\tau = k_\tau \frac{\mathbf{J} \hat{\psi}_s}{\|\hat{\psi}_s\|} \quad (5c)$$

where k_ψ and k_τ are scalar gains and $\hat{\mathbf{i}}_a$ is the auxiliary current estimate. The scalar gains are related to closed-loop bandwidths, i.e.,

$$k_\psi = \frac{\alpha_\psi \|\hat{\mathbf{i}}_a\| \|\hat{\psi}_s\|}{\hat{\mathbf{i}}_a^T \hat{\psi}_s} \quad k_\tau = \frac{\alpha_\tau \|\hat{\psi}_s\|}{\hat{\mathbf{i}}_a^T \hat{\psi}_s} \quad (5d)$$

where α_ψ is the flux-control bandwidth and α_τ is the torque-control bandwidth. If desired, these relations allow selecting constant bandwidths. Alternatively, if constant gains k_ψ and k_τ are used, the bandwidths depend on the operating point according to (5d).

A transparent current controller can be embedded into the control law (5b) by replacing it with

$$\mathbf{e}_s = \alpha_c \hat{\mathbf{L}}_s (\bar{\mathbf{i}}_{s,\text{ref}} - \mathbf{i}_s) \quad (6a)$$

where α_c is the current-control bandwidth and $\bar{\mathbf{i}}_{s,\text{ref}} = \text{sat}(\mathbf{i}_{s,\text{ref}})$ is the limited internal current reference. The unlimited reference is

$$\mathbf{i}_{s,\text{ref}} = \mathbf{i}_s + \frac{\hat{\mathbf{L}}_s^{-1}}{\alpha_c} \left[\mathbf{k}_\psi (\psi_{s,\text{ref}} - \hat{\psi}_s) + \mathbf{k}_\tau (\tau_{m,\text{ref}} - \hat{\tau}_m) \right]. \quad (6b)$$

It can be seen that if the current reference is not limited, i.e., $\bar{\mathbf{i}}_{s,\text{ref}} = \mathbf{i}_{s,\text{ref}}$ holds, this control law equals (5b). Furthermore, if desired, the current control mode is available through $\bar{\mathbf{i}}_{s,\text{ref}}$.

It can be shown that the control law (5) equals the one presented in [16], except that the integrators in the control law are omitted here for simplicity. This allows to omit the antiwindup mechanism and to create a link between flux-vector control and observer-based V/Hz control.

B. State Observer

Based on the model (2), a nonlinear state observer can be formed [24]

$$\frac{d\hat{\psi}_s}{dt} = \mathbf{e}_s - (\omega_s - \hat{\omega}_m) \mathbf{J} \hat{\psi}_s + \mathbf{K}_\psi \mathbf{e}_\psi \quad (7a)$$

$$\frac{d\hat{\vartheta}_m}{dt} = \hat{\omega}_m + \mathbf{k}_\delta^T \mathbf{e}_\psi = \omega_s \quad (7b)$$

where the estimates are marked with the hat. For compactness, the observer is expressed using the control error term (5b), instead of the stator voltage in (5a).² The correction vector

$$\mathbf{e}_\psi = \hat{\psi}_f + \hat{\mathbf{L}}_s \mathbf{i}_s - \hat{\psi}_s \quad (7c)$$

can be interpreted as the error of the observed stator flux with respect to the flux estimate based on the model (2c), or, equivalently, the estimation error of the stator

²Here, the observer is presented in a different form as compared to [24], where the PI mechanism was used for the rotor angle and speed estimation.

current scaled by the stator inductance estimate. The torque estimate is defined by

$$\hat{\tau}_m = (\mathbf{J}\hat{\psi}_s)^T \mathbf{i}_s. \quad (7d)$$

The observer gain matrix and the gain vector, respectively, are

$$\mathbf{K}_\psi = b \frac{\hat{\psi}_a \hat{\psi}_a^T}{\|\hat{\psi}_a\|^2} \quad \mathbf{k}_\delta^T = -\alpha_\delta \frac{(\mathbf{J}\hat{\psi}_a)^T}{\|\hat{\psi}_a\|^2} \quad (7e)$$

where the positive parameter b determines the damping of the flux estimation error and α_δ is the rotor-angle estimation bandwidth. The auxiliary flux and the auxiliary current, respectively, are

$$\hat{\psi}_a = \hat{\psi}_f + (\hat{\mathbf{L}}_s + \mathbf{J}\hat{\mathbf{L}}_s\mathbf{J})\mathbf{i}_s \quad (7f)$$

$$\hat{\mathbf{i}}_a = -\mathbf{J}\hat{\mathbf{L}}_s^{-1}\mathbf{J}\hat{\psi}_a. \quad (7g)$$

The auxiliary flux reduces to $\hat{\psi}_a = \hat{\psi}_f$ if $L_d = L_q$. The gains in (7e) decouple the flux estimation from the rotor-angle estimation [24]. If desired, the observer could be extended with PM flux estimation [25]. The state observer is locally stable in every operating point, except at zero frequency, where it is marginally stable, as shown in Appendix B.³ For prolonged stable operation at very low speeds under load and parameter variations, the observer can be extended with signal injection [28], [29].

C. Control Configurations

Fig. 2 shows three different control configurations of flux-vector control. These configurations are described in the following and analyzed in detail in Section IV.

1) *Sensored Speed Control*: Fig. 2(a) shows a speed-control configuration with feedback from the measured speed. A two-degrees-of-freedom (2DOF) PI speed controller is considered as an example. It can be represented using the disturbance-observer structure

$$\frac{d\tau_i}{dt} = \alpha_i(\bar{\tau}_{m,\text{ref}} - \hat{\tau}_L) \quad (8a)$$

$$\hat{\tau}_L = \tau_i - (k_p - k_t)\omega_m \quad (8b)$$

$$\tau_{m,\text{ref}} = k_t(\omega_{m,\text{ref}} - \omega_m) + \hat{\tau}_L \quad (8c)$$

where $\bar{\tau}_{m,\text{ref}}$ is the realized (limited) torque reference, k_t is the reference-feedforward gain, k_p is the proportional gain, $\alpha_i = k_i/k_t$ is the inverse of the integral time, and $\hat{\tau}_L$ is the input-equivalent disturbance estimate, i.e., the load torque estimate. Setting $k_t = k_p$ yields the standard PI controller.

2) *Sensorless Speed Control*: If the measured speed is not available, the speed can be estimated, as shown in Fig. 2(b). In this case, the state observer is extended with the speed estimation

$$\frac{d\hat{\omega}_m}{dt} = \mathbf{k}_\omega^T \mathbf{e}_\psi \quad (9)$$

³It is worth noticing that the global stability proof presented in [26] can be extended to the observer (7), see Remark 2 in [26]. The control law (5) is also globally valid. However, the separation principle is not generally valid for nonlinear systems [27].

where \mathbf{k}_ω^T is the gain vector. To avoid coupling with the flux estimation, the gain vector \mathbf{k}_ω^T should be parallel with \mathbf{k}_δ^T , whose direction is given in (7e). The selection $\mathbf{k}_\omega^T = (\alpha_\delta/4)\mathbf{k}_\delta^T$ results in the speed-estimation bandwidth $\alpha_\omega = \alpha_\delta/2$. The speed estimator (9) can be interpreted as a disturbance observer, where the disturbance model is $d\omega_m/dt = 0$. The speed controller (8) can be used in the sensorless case as well.

3) *V/Hz Control*: Fig. 2(c) shows the V/Hz control configuration. In this case, neither the speed controller nor the speed estimator is needed. Instead, the torque reference is obtained simply by low-pass filtering the torque estimate

$$\frac{d\tau_{m,\text{ref}}}{dt} = \alpha_f(\hat{\tau}_m - \tau_{m,\text{ref}}) \quad (10)$$

where α_f is the low-pass filter bandwidth. Furthermore, the speed estimate for the state observer is the quasi-constant speed reference, i.e., $\hat{\omega}_m = \omega_{m,\text{ref}}$. Unlike in the speed-control configurations, the speed reference has to be rate-limited in V/Hz control.

IV. ANALYSIS

The control system in Section III has been derived using nonlinear models and control methods. The purpose of the following small-signal analysis is to give further insight to the drive system for the practitioner. Fig. 3 illustrates the linearized closed-loop system consisting of the machine model (2), the control law (5), and the state observer (7). Its state-space representation is derived in Appendix B, from which the expressions presented in this section originate. The inverter is assumed to be ideal, i.e., $\mathbf{u}_s = \mathbf{u}_{s,\text{ref}}$, and parameter errors are omitted. Using the stator current as an example, the small-signal deviation about the operating point is denoted by $\Delta\mathbf{i}_s = \mathbf{i}_s - \mathbf{i}_{s0}$, where \mathbf{i}_{s0} is the operating-point quantity. Other small-signal and operating-point quantities are marked similarly.

A. State Observer

1) *Flux Observer*: The estimation-error dynamics, obtained from the machine model (2) and the state observer (7), are linearized. With the selected observer design, the flux-estimation dynamics are decoupled from the remaining control system, as illustrated in Fig. 3 and shown in Appendix B. Consequently, the flux estimation error $\Delta\tilde{\psi}_s = \Delta\psi_s - \Delta\hat{\psi}_s$ acts only as an external disturbance to the control system and is omitted in the following with no loss of generality.

2) *Position Observer*: In the Laplace domain, the dynamics of the rotor angle estimation error are

$$\Delta\tilde{\vartheta}_m(s) = \frac{1}{s + \alpha_\delta} [\Delta\omega_m(s) - \Delta\hat{\omega}_m(s)]. \quad (11)$$

These angle-tracking dynamics are of the first order.

B. Speed Estimation

Using the linearized form of the speed estimation (9), the rotor speed estimate can be expressed in the Laplace domain

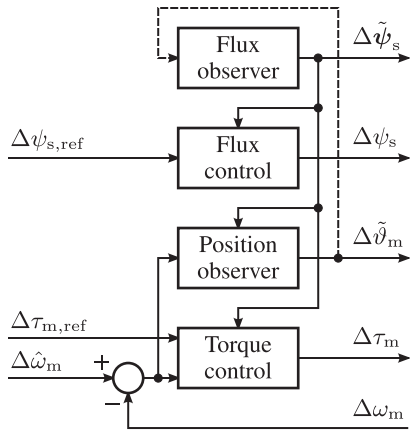


Fig. 3. Linearized model of the closed-loop system consisting of the machine model (2), the control law (5), and the state observer (7). Mechanical impedance is the transfer function from the actual rotor speed $\Delta\omega_m$ to the electromagnetic torque $\Delta\tau_m$. Coupling from the position observer to the flux observer (shown by the dashed line) is removed by means of the observer design. Consequently, the flux-estimation error $\Delta\psi_s$ appears as an external disturbance. Note that even though the actual rotor speed is not measured in sensorless control, it appears as an input in the linearized model.

as $\Delta\hat{\omega}_m(s) = (\alpha_\omega^2/s)\Delta\tilde{\vartheta}_m(s)$, where $\alpha_\omega = \alpha_\delta/2$ is the speed-estimation bandwidth. Combining this expression with (11) yields the transfer function from the rotor speed to its estimate

$$G_\omega(s) = \frac{\Delta\hat{\omega}_m(s)}{\Delta\omega_m(s)} = \frac{\alpha_\omega^2}{(s + \alpha_\omega)^2} \quad (12)$$

which affects the torque-control loop dynamics in sensorless flux-vector control.

C. Flux-Control Loop

The machine model (2) and the control law (5) result in the following closed-loop flux dynamics

$$\frac{\Delta\psi_s(s)}{\Delta\psi_{s,ref}(s)} = \frac{\alpha_\psi}{s + \alpha_\psi}. \quad (13)$$

The flux dynamics are decoupled from the torque dynamics and valid regardless of the speed control strategy.

D. Torque-Control Loop

In the study of the torque dynamics, the transfer function from the rotor speed to the electromagnetic torque, i.e., the mechanical impedance

$$Z_m(s) = -\frac{\Delta\tau_m(s)}{\Delta\omega_m(s)}. \quad (14)$$

is of particular interest [30]. The mechanical impedance depends on the electromagnetic subsystem and the control system. Its counterpart is the transfer function from the electromagnetic torque to the rotor speed, i.e., the mechanical subsystem $M(s) = \Delta\omega_m(s)/\Delta\tau_m(s)$. In the simplest case

$$M(s) = \frac{1}{Js} \quad (15)$$

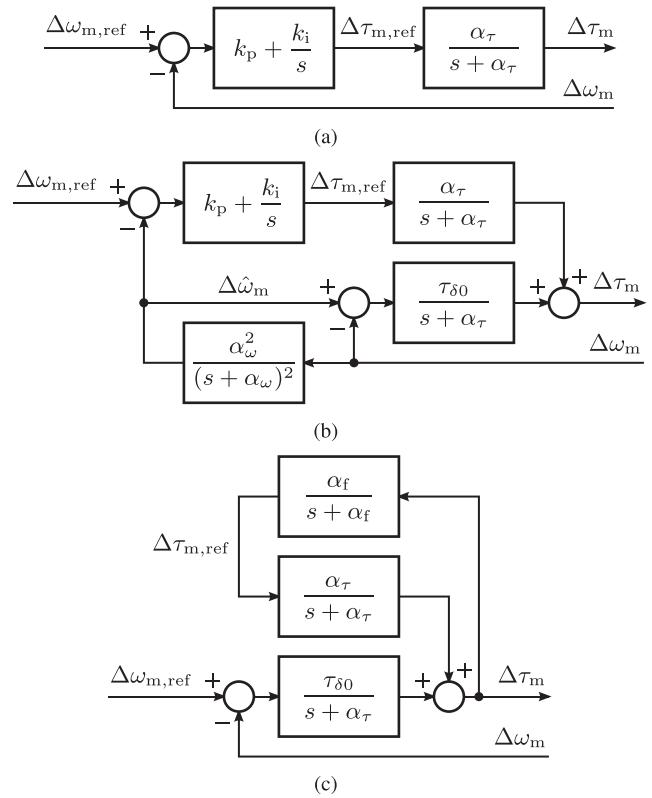


Fig. 4. Linearized models for the mechanical impedance: (a) sensed; (b) sensorless; and (c) V/Hz control configuration. (a) and (b) Reference feedforward of the speed controller is not shown since it does not affect the mechanical impedance.

where J is the total inertia. The closed-loop poles of torque-control loop can be obtained by solving

$$1 + Z_m(s)M(s) = 0. \quad (16)$$

The mechanical subsystem may be unknown, especially in the case of V/Hz control. The concept of passivity can be used to stabilize the closed-loop system without the knowledge on the mechanical subsystem. The mechanical impedance is passive if

$$\text{Re}\{Z_m(j\omega)\} \geq 0. \quad (17)$$

holds for all frequencies ω [23]. The passivity is sufficient but not necessary condition for the stability. The negative feedback interconnection of two passive systems is also passive. The mechanical subsystem can typically be assumed to be passive. Hence, the passivity of the mechanical impedance is of interest, particularly for V/Hz control.

In the following, the mechanical impedances and the passivity conditions are analyzed for three control configurations shown in Fig. 4.

1) *Sensed Flux-Vector Control*: Fig. 4(a) shows the linearized model for the mechanical impedance in the case of the speed-sensed control configuration, which has been derived from the linearized model by assuming $\hat{\omega}_m = \omega_m$. In the

Laplace domain, the speed controller (8) is

$$\Delta\tau_{m,\text{ref}}(s) = (k_t - k_p)\Delta\omega_{m,\text{ref}}(s) + K(s)[\Delta\omega_{m,\text{ref}}(s) - \Delta\omega_m(s)] \quad (18)$$

where

$$K(s) = k_p + k_i/s \quad (19)$$

is the feedback controller. Furthermore, the transfer function from the torque reference to the electromagnetic torque is (Appendix B)

$$K_\tau(s) = \frac{\Delta\tau_m(s)}{\Delta\tau_{m,\text{ref}}(s)} = \frac{\alpha_\tau}{s + \alpha_\tau}. \quad (20)$$

The torque dynamics are

$$\Delta\tau_m(s) = Z_\omega(s)\Delta\omega_{m,\text{ref}}(s) - Z_m(s)\Delta\omega_m(s) \quad (21)$$

where the transfer function $Z_\omega(s) = K_\tau(s)(k_t + k_i/s)$ governs the torque response from the speed reference. The mechanical impedance is

$$Z_m(s) = K_\tau(s)K(s). \quad (22)$$

It can be shown that passivity condition for (22) with positive design parameters α_τ , k_p , and k_i is

$$\frac{k_i}{k_p} < \alpha_\tau \quad (23)$$

which holds if the tuning of the speed controller is reasonable.

2) *Sensorless Flux-Vector Control*: Fig. 4(b) shows the linearized model for sensorless flux-vector control. The mechanical impedance is derived by applying the speed controller (18) and the observer dynamics (12), resulting in⁴

$$Z_m(s) = \frac{\tau_{\delta 0}}{s + \alpha_\tau} [1 - G_\omega(s)] + K_\tau(s)K(s)G_\omega(s). \quad (24)$$

The mechanical impedance is passive if

$$k_p < \frac{\tau_{\delta 0}}{\alpha_\tau} + \frac{2\tau_{\delta 0} + k_i}{2\alpha_\omega + \alpha_\tau} \quad \frac{k_i}{k_p} < \frac{\alpha_\omega \alpha_\tau}{\alpha_\omega + 2\alpha_\tau}. \quad (25)$$

These conditions are difficult to meet in practice, without making either the speed controller or the torque controller sluggish. However, as mentioned earlier, passivity is not a necessary condition for stability. For a rigid mechanical system, the stable closed-loop system can be easily achieved, if the inertia is known.

3) *V/Hz Control*: Fig. 4(c) shows the linearized model for the V/Hz control configuration. The resulting mechanical impedance is

$$Z_m(s) = \frac{s + \alpha_f}{s + \alpha_\tau + \alpha_f} \frac{\tau_{\delta 0}}{s}. \quad (26)$$

The torque dynamics are

$$\Delta\tau_m(s) = Z_m(s)[\Delta\omega_{m,\text{ref}}(s) - \Delta\omega_m(s)]. \quad (27)$$

⁴By omitting the speed controller, the control system operates in the torque control mode. The mechanical impedance becomes $Z_m(s) = \tau_{\delta 0}/(s + \alpha_\tau)[1 - G_\omega(s)]$. It can be easily shown that flux-vector control is passive in the torque control mode. In the case of sensed drive, $G_\omega(s) = 1$ and the mechanical impedance reduces to $Z_m(s) = 0$.

TABLE I
DESIGN PARAMETERS

Flux observer	
Angle-estimation bandwidth α_δ	$2\pi \cdot 80$ rad/s
Damping parameter b	(28)
Flux-vector control	
Flux-control bandwidth α_ψ	$2\pi \cdot 100$ rad/s
Torque-control bandwidth α_τ	$2\pi \cdot 100$ rad/s
Speed-control bandwidth α_s	$2\pi \cdot 4$ rad/s
k_t, k_p, α_i	$\alpha_s J, 2\alpha_s J, \alpha_s$
Speed-estimation bandwidth α_ω	$2\pi \cdot 40$ rad/s
V/Hz control	
Flux-control bandwidth α_ψ	$2\pi \cdot 100$ rad/s
Torque-control bandwidth α_τ	$2\pi \cdot 20$ rad/s
Low-pass filter bandwidth α_f	$2\pi \cdot 1$ rad/s

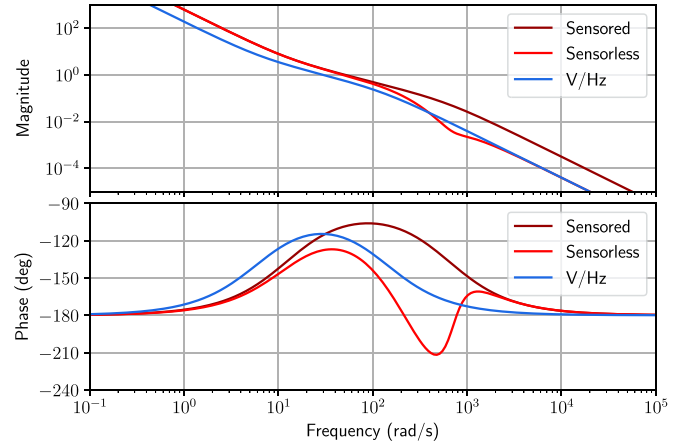


Fig. 5. Frequency response of the loop gain $Z_m(s)M(s)$ for sensed, sensorless, and V/Hz control configurations.

With positive design parameters α_τ and α_f , the mechanical impedance is passive in the feasible operating region where $\tau_{\delta 0} > 0$. Consequently, the V/Hz control configuration is locally stable for any passive mechanics, as expected based on [22].

4) *Numerical Analysis of the Closed-Loop System*: The closed-loop torque control is illustrated with a frequency response graph. The design parameters given in Table I are used in this example. The used torque factor $\tau_{\delta 0}$ corresponds to the rated flux magnitude and the rated torque.

Fig. 5 shows the frequency response of the loop gain $Z_m(s)M(s)$, which can be used to assess the stability of the closed-loop system. As expected from the analysis, the phase of the loop gain never goes below -180° in the case of sensed and V/Hz control, corresponding to the passivity condition in (17). The sensorless case is not passive but still stable: the gain margin is 8.5 dB and the phase margin 52° . Increasing the speed-estimation bandwidth α_ω or decreasing the speed-control bandwidth α_s would further increase these margins. Conversely, the opposite adjustments would eventually result in an unstable closed-loop system.

V. IMPLEMENTATION ASPECTS

A. State Observer

The damping parameter for the observer gain in (7e) is scheduled as

$$b = 2\zeta_\infty |\hat{\omega}_m| + \frac{R_s}{2} \left(\frac{1}{L_d} + \frac{1}{L_q} \right) \quad (28)$$

where ζ_∞ is the desired damping ratio at high speeds. At high speeds, the observer poles are located at $s = -(\zeta_\infty \pm j\sqrt{1 - \zeta_\infty^2})|\omega_{m0}|$. At zero speed $\omega_{m0} = 0$, the latter term in (28) results in the poles being located at $s = 0$ and $s = -R_s(L_d + L_q)/(2L_dL_q)$. Thus, double poles at the origin $s = 0$ are avoided, which would prevent magnetizing and starting of the machine in a stable manner.

The studied SyRM exhibits considerable saturation characteristics, which are taken into account in the state observer using an algebraic inductance model [31], [32]

$$L_d(\hat{\psi}_d, \hat{\psi}_q) = \frac{1}{a_d + a_{dd}|\hat{\psi}_d|^S + \frac{a_{dq}}{V+2}|\hat{\psi}_d|^U|\hat{\psi}_q|^{V+2}} \quad (29a)$$

$$L_q(\hat{\psi}_d, \hat{\psi}_q) = \frac{1}{a_q + a_{qq}|\hat{\psi}_q|^T + \frac{a_{dq}}{U+2}|\hat{\psi}_d|^{U+2}|\hat{\psi}_q|^V} \quad (29b)$$

where $\hat{\psi}_d$ and $\hat{\psi}_q$ are the d- and q-axis components of the stator flux estimate. In the model, the exponents $S = 5$, $T = 1$, $U = 1$, and $V = 0$ are used. The coefficients $a_d = 0.36$ p.u. and $a_q = 1.08$ p.u. are the inverses of the unsaturated d- and q-axis inductances, respectively. Self-axis saturation is considered by the coefficients $a_{dd} = 0.15$ p.u. and $a_{qq} = 6.20$ p.u. The coefficient $a_{dq} = 2.18$ p.u. takes cross-saturation into account. The graphical form of the flux maps of this machine is available in [33].

B. Reference Generation

The reference for the stator flux magnitude can be pre-computed offline [34] or adapted online [18]. In this work, the feedforward field-weakening scheme in [33] is used and briefly presented here for completeness. The method includes the maximum-torque-per-ampere (MTPA) locus and MTPV limits. Magnetic saturation is considered in the computation of the look-up tables. If desired, the iron losses could be also included in reference generation, see e.g., [35], but are omitted here for the sake of simplicity.

The optimal stator flux reference is the output of the look-up table, which implements the MTPA condition for a given torque reference, i.e.,

$$\psi_{\text{mtpa}} = \psi_{\text{mtpa}}(\tau_{\text{m,ref}}). \quad (30a)$$

The maximum stator flux magnitude is limited by the dc-bus voltage u_{dc} and the stator frequency,

$$\psi_{\text{max}} = \frac{k_u u_{\text{dc}}}{\sqrt{3}\hat{\omega}_m} \quad (30b)$$

where the factor k_u defines the voltage margin. The stator flux reference and the limited torque reference are obtained as

$$\psi_{\text{s,ref}} = \min(\psi_{\text{mtpa}}, \psi_{\text{max}}) \quad (30c)$$

TABLE II
DATA OF THE 6.7-kW FOUR-POLE SYRM

Rated values		
Voltage (line-to-neutral, peak value)	$\sqrt{2/3} \cdot 370$ V	1 p.u.
Current (peak value)	$\sqrt{2} \cdot 15.5$ A	1 p.u.
Frequency	105.8 Hz	1 p.u.
Speed	3 175 r/min	1 p.u.
Torque	20.1 Nm	0.67 p.u.
Parameters		
Stator resistance R_s	0.55 Ω	0.04 p.u.
d-axis inductance L_d	46 mH	2.20 p.u.
q-axis inductance L_q	6.8 mH	0.33 p.u.
Total inertia J	0.015 kgm ²	110.9 p.u.

TABLE III
DATA OF THE 2.2-kW SIX-POLE INTERIOR PM SYNCHRONOUS MACHINE

Rated Values		
Voltage (line-to-neutral, peak value)	$\sqrt{2/3} \cdot 370$ V	1 p.u.
Current (peak value)	$\sqrt{2} \cdot 4.3$ A	1 p.u.
Frequency	75 Hz	1 p.u.
Speed	1 500 r/min	1 p.u.
Torque	14 Nm	0.80 p.u.
Parameters		
Stator resistance R_s	3.6 Ω	0.07 p.u.
d-axis inductance L_d	36 mH	0.36 p.u.
q-axis inductance L_q	51 mH	0.48 p.u.
PM flux linkage ψ_f	0.55 Vs	0.85 p.u.
Total inertia J	0.015 kgm ²	63.3 p.u.

$$\bar{\tau}_{\text{m,ref}} = \text{sign}(\tau_{\text{m,ref}}) \cdot \min(|\tau_{\text{m,ref}}|, \tau_{\text{max}}) \quad (30d)$$

where $\tau_{\text{max}} = \tau_{\text{max}}(\psi_{\text{s,ref}})$ is the maximum operating-point torque under the combined MTPV and current limit constraints, implemented using another look-up table.

VI. RESULTS

The sensorless flux-vector control is studied by means of experiments using two example machines, a 6.7-kW four-pole SyRM and a 2.2-kW six-pole interior PM machine. The data for these two machines are given in Tables II and III. The design parameters used in the experiments correspond to those in Table I.

The experimental setup is shown in Fig. 6. The controller is implemented on a dSPACE MicroLabBox rapid prototyping system. The switching-state signals from the prototyping system are directly used by the commercially available inverter, bypassing its own control board. The switching frequency is 5 kHz, and double sampling is used. Inverter nonlinearities are compensated for using a simple current feedforward method. The load drive uses a commercial vector controller in torque control mode. The rotor speed is measured using a resolver only for monitoring purposes.

The experimental result in Fig. 7 showcases the speed control mode using the SyRM. The test sequence considers a fast stepwise change of the speed reference from 0 to 1.75 p.u. During the acceleration, the torque reference $\tau_{\text{m,ref}}$ and stator flux reference $\psi_{\text{s,ref}}$ remain constant in the base-speed region

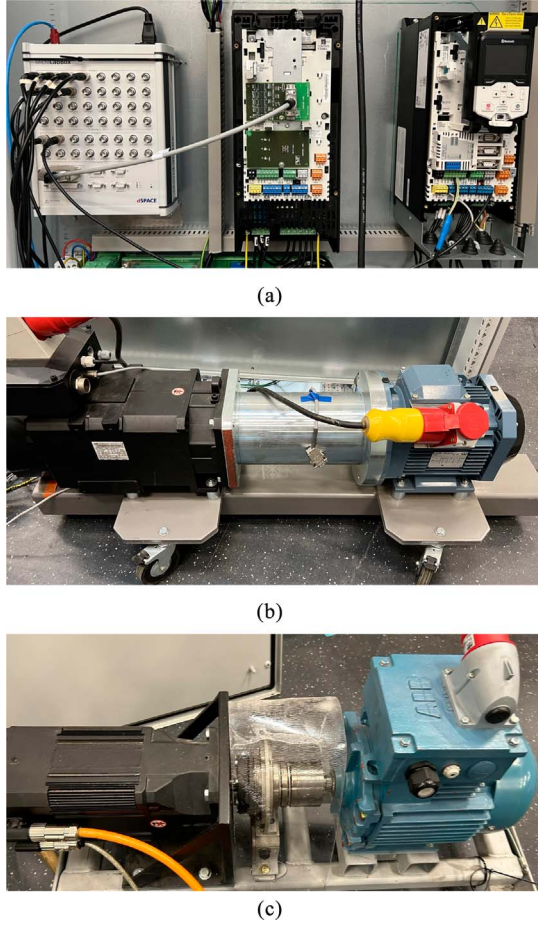


Fig. 6. Experimental setup: (a) rapid prototyping system and frequency converters; (b) SyRM bench; and (c) PM machine bench. (a) dSPACE MicroLabBox prototyping system is on the left, the frequency converter for the machine under test is in the center, and the frequency converter for the load machine is on the right. (b) Induction machine used as a load is on the left, and the 6.7-kW SyRM is on the right. (c) 2.2-kW PM machine is on the right.

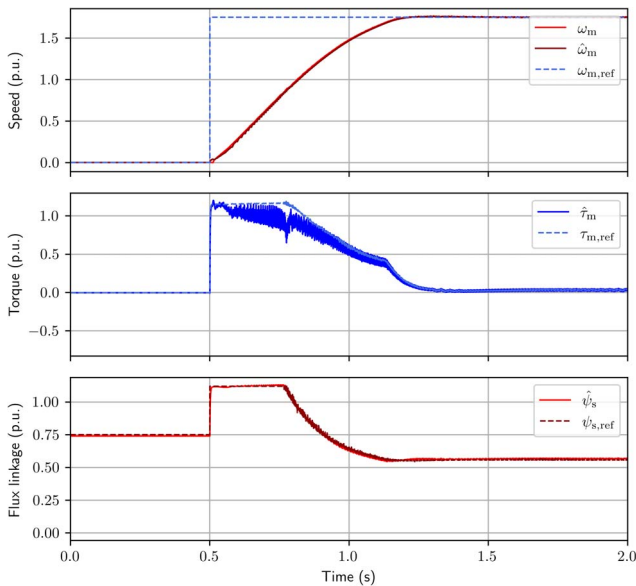


Fig. 7. Experimental result showing acceleration with the SyRM in the speed control mode with a speed reference step from 0 to 1.75 p.u.

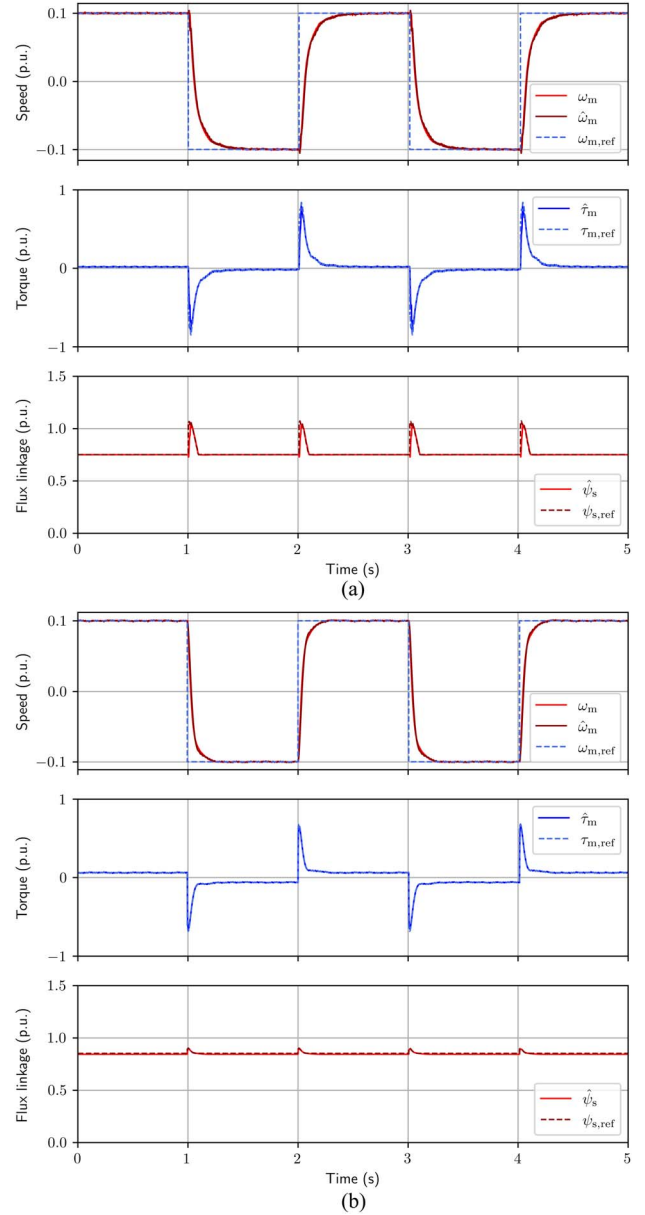


Fig. 8. Experimental result showing speed reversals in the speed control mode with: (a) SyRM; (b) PM machine. The reference speed is changed stepwise between 0.1 p.u. and -0.1 p.u.

according to the MTPA locus. In the field-weakening region, the control variables are bounded by the current limit and the MTPV limit.

Fig. 8(a) shows experimental results at low speeds for the speed-control mode for the SyRM. The speed reference is changed stepwise between 0.1 and -0.1 p.u. Fig. 8(b) shows the same test for the PM machine. In Fig. 8(b), the rise-time of 0.09 s corresponds to the desired speed-control bandwidth of $2\pi \cdot 4$ rad/s. For the SyRM, the actual speed-control bandwidth is slightly lower than designed due to parameter estimate inaccuracies.

Fig. 9(a) shows an experimental result with the PM machine at the rated speed with the speed control mode. The machine is accelerated from 0 to 1 p.u. followed by load steps of the

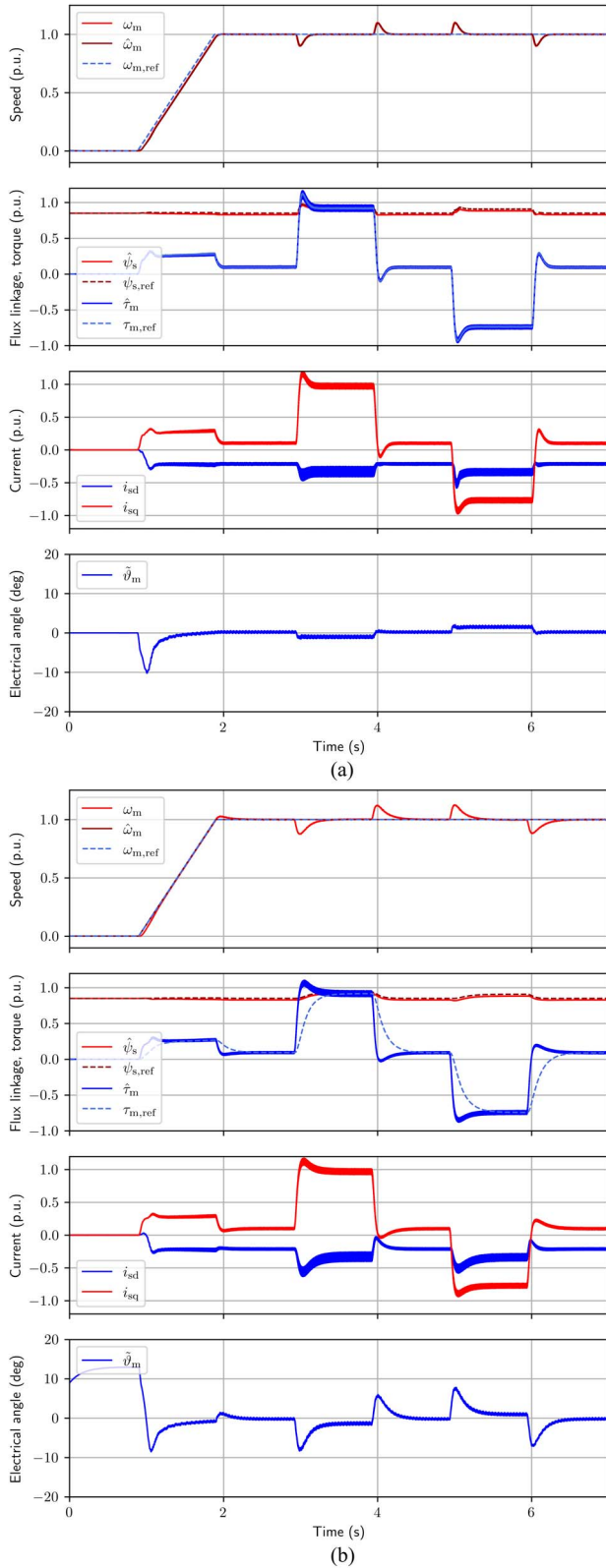


Fig. 9. Experimental results showing operation at the rated speed for the PM machine in: (a) speed control mode; (b) V/Hz control mode. Speed reference is ramped to 1 p.u. after $t = 1$ s and load torque steps of the rated torque (0.80 p.u.) are applied in positive and negative directions at $t = 3$ s and $t = 5$ s, respectively.

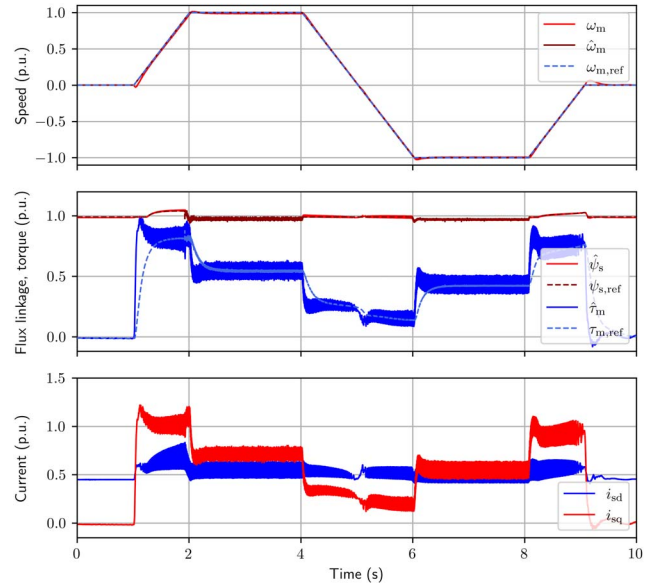


Fig. 10. Experimental result for the SyRM showing acceleration and deceleration under the rated torque (0.67 p.u.) in the V/Hz control mode. Constant flux reference $\psi_{s,ref}$ and constant inductance estimates L_d and L_q are used.

rated torque applied in the positive and negative directions at $t = 3$ s and $t = 5$ s, respectively. Fig. 9(b) shows the same test sequence for the V/Hz control mode. The fourth subplot in these figures shows the angle estimation error $\tilde{\vartheta}_m = \vartheta_m - \hat{\vartheta}_m$, i.e., the error between the estimated and real position. In Fig. 9(b), the initial angle estimate is erroneous, but the control system is able to recover. As expected from the analysis in Section IV, the system in the V/Hz control mode is stable and well damped. The angle estimation error subplot also indirectly illustrates the voltage-source behavior of the V/Hz control configuration.

Fig. 10 showcases the robustness against parameter uncertainties of the V/Hz control mode with acceleration and deceleration under the rated load torque. In this test, the inductance model (29) is replaced with the constant inductance estimates in Table II. The speed reference is increased from 0 to 1 p.u., then reversed, and finally brought back to zero. The load torque is applied from the beginning of the acceleration until the end of the sequence. Constant flux-magnitude reference is used to minimize effects of the unmodeled saturation.

VII. CONCLUSION

A design framework for sensorless control of synchronous machines is presented, using flux-vector control as the base method. The observer-based V/Hz control mode can be presented in the same framework. The sensorless flux-vector control was systematically analyzed. The developed linearized models for the mechanical impedance can be used for stability analysis. Passivity conditions for the mechanical impedance were also derived, which can be utilized for unknown or resonant, but passive, mechanical loads. Sensorless flux-vector control and observer-based V/Hz control were experimentally evaluated using a 6.7-kW SyRM and a 2.2-kW PM machine.

APPENDIX A MTPA AND MTPV CONDITIONS

Consider the magnetic model (2c) in the form $\psi_s(i_s, \delta) = \psi_f(\delta) + \mathbf{L}_s(\delta)\mathbf{i}_s$. Using (2d), the partial derivative of the torque with respect to the load angle is

$$\frac{\partial \tau_m(i_s, \delta)}{\partial \delta} = \left[\mathbf{J} \frac{\partial \psi_s(i_s, \delta)}{\partial \delta} \right]^T \mathbf{i}_s = \psi_a^T \mathbf{i}_s \quad (31)$$

where the auxiliary flux is defined by [24]

$$\psi_a = \mathbf{J} \frac{\partial \psi_s(i_s, \delta)}{\partial \delta} = \psi_s + \mathbf{J} \mathbf{L}_s(\delta) \mathbf{J} \mathbf{i}_s \quad (32)$$

Hence, the MTPA condition can be written as $\psi_a^T \mathbf{i}_s = 0$ [36]. For nonsalient machines, the auxiliary flux reduces to the PM flux, i.e., $\psi_a = \psi_f(\delta)$.

To derive the MTPV condition, the torque in (2d) can be expressed as a function of the stator flux using (2c), resulting in

$$\frac{\partial \tau_m(\psi_s, \delta)}{\partial \delta} = (\mathbf{J} \psi_s)^T \frac{\partial \mathbf{i}_s(\psi_s, \delta)}{\partial \delta} = \mathbf{i}_a^T \psi_s \quad (33)$$

where the auxiliary current is defined by

$$\mathbf{i}_a = -\mathbf{J} \frac{\partial \mathbf{i}_s(\psi_s, \delta)}{\partial \delta} = -\mathbf{i}_s - \mathbf{J} \mathbf{L}_s^{-1}(\delta) \mathbf{J} \psi_s. \quad (34)$$

Consequently, the MTPV condition is $\mathbf{i}_a^T \psi_s = 0$. It can also be noticed that the auxiliary flux can be expressed using the auxiliary current, $\psi_a = -\mathbf{J} \mathbf{L}_s(\delta) \mathbf{J} \mathbf{i}_a$.

APPENDIX B LINEARIZED MODEL

The core of the linearized model is the same for all control configurations. The model for the V/Hz control configuration is obtained by substituting $\Delta \hat{\omega}_m = \Delta \omega_{m,\text{ref}}$.

A. State Observer

Linearization of the error vector of (7c) gives

$$\Delta e_\psi = \Delta \tilde{\psi}_s - \mathbf{J} \psi_{a0} \Delta \tilde{\vartheta}_m \quad (35)$$

where $\Delta \tilde{\psi}_s = \Delta \psi_s - \Delta \hat{\psi}_s$ is the linearized flux estimation error about an operating point. Other estimation errors are defined similarly. The last term in (35) originates from the angle-dependent stator inductance and PM flux in (1). Note that $\Delta \tilde{\vartheta}_m = \Delta \vartheta_m - \Delta \hat{\vartheta}_m = \Delta \delta - \Delta \hat{\delta} = \Delta \tilde{\delta}$.

Using (2), (7), and (35), the linearized estimation-error dynamics are obtained

$$\frac{d\tilde{\psi}_s}{dt} = -(\omega_{m0} \mathbf{J} + \mathbf{K}_{\psi 0}) \Delta \tilde{\psi}_s + \mathbf{K}_{\psi 0} \mathbf{J} \psi_{a0} \Delta \tilde{\vartheta}_m \quad (36a)$$

$$\frac{d\tilde{\vartheta}_m}{dt} = -\mathbf{k}_{\delta 0}^T \Delta \tilde{\psi}_s + \mathbf{k}_{\delta 0}^T \mathbf{J} \psi_{a0} \Delta \tilde{\vartheta}_m + \Delta \omega_m - \Delta \hat{\omega}_m \quad (36b)$$

$$\Delta \tilde{\tau}_m = \mathbf{i}_{s0}^T \mathbf{J} \Delta \tilde{\psi}_s \quad (36c)$$

where the operating-point gains are

$$\mathbf{K}_{\psi 0} = b \frac{\psi_{a0} \psi_{a0}^T}{\|\psi_{a0}\|^2} \quad \mathbf{k}_{\delta 0}^T = -\alpha_\delta \frac{(\mathbf{J} \psi_{a0})^T}{\|\psi_{a0}\|^2}. \quad (36d)$$

Since $\mathbf{K}_{\psi 0} \mathbf{J} \psi_{a0} = \mathbf{0}$, the flux estimation dynamics are decoupled from the remaining system. The resulting observer characteristic polynomial is $(s + \alpha_\delta)(s^2 + bs + \omega_{m0}^2)$. The transfer function (11) is obtained from (36b).

B. Speed Estimation

The linearized form of the speed estimator (9) is

$$\frac{d\Delta \hat{\omega}_m}{dt} = \mathbf{k}_{\omega 0}^T \Delta \tilde{\psi}_s - \mathbf{k}_{\omega 0}^T \mathbf{J} \psi_{a0} \Delta \tilde{\vartheta}_m \quad (37)$$

where the gain is $\mathbf{k}_{\omega 0}^T = (\alpha_\omega/4) \mathbf{k}_{\delta 0}^T$. With the speed estimator, the observer characteristic polynomial is $(s + \alpha_\omega)^2(s^2 + bs + \omega_{m0})$, where $\alpha_\omega = \alpha_\delta/2$ is the speed-estimation bandwidth. The transfer function (12) is obtained from (36b) to (37).

C. Control Law

Assuming an ideal inverter and accurate parameter estimates, the machine model in (2) and the control law in (5) result in the nonlinear closed-loop dynamics

$$\begin{aligned} \frac{d\psi_s}{dt} &= \frac{\psi_s^T \mathbf{k}_\psi (\psi_{s,\text{ref}} - \hat{\psi}_s) + \psi_s^T \mathbf{k}_\tau (\tau_{m,\text{ref}} - \hat{\tau}_m)}{\|\psi_s\|} \\ &\quad + \frac{\hat{\omega}_m \psi_s^T \mathbf{J} \hat{\psi}_s}{\|\psi_s\|} \end{aligned} \quad (38a)$$

$$\begin{aligned} \frac{d\tau_m}{dt} &= (\mathbf{J} \mathbf{i}_a)^T [\mathbf{k}_\psi (\psi_{s,\text{ref}} - \hat{\psi}_s) \\ &\quad + \mathbf{k}_\tau (\tau_{m,\text{ref}} - \hat{\tau}_m) + \hat{\omega}_m \mathbf{J} \hat{\psi}_s - \omega_m \mathbf{J} \psi_s]. \end{aligned} \quad (38b)$$

Linearization results in

$$\frac{d\Delta \psi_s}{dt} = \alpha_\psi (\Delta \psi_{s,\text{ref}} - \Delta \psi_s) + \beta_{\psi 0}^T \Delta \tilde{\psi}_s \quad (39a)$$

$$\begin{aligned} \frac{d\Delta \tau_m}{dt} &= \alpha_\tau (\Delta \tau_{m,\text{ref}} - \Delta \tau_m) + \tau_{\delta 0} (\Delta \hat{\omega}_m - \Delta \omega_m) \\ &\quad + \beta_{\tau \psi 0}^T \Delta \tilde{\psi}_s \end{aligned} \quad (39b)$$

where the parameters $\beta_{\psi 0}^T$ and $\beta_{\tau \psi 0}^T$ are not of interest, since the flux estimation error $\Delta \tilde{\psi}_s$ is decoupled from the remaining system with the used observer design, see (36). The transfer functions in Section IV-D are obtained from (39).

REFERENCES

- [1] S. Morimoto, M. Sanada, and Y. Takeda, "Wide-speed operation of interior permanent magnet synchronous motors with high-performance current regulator," *IEEE Trans. Ind. Appl.*, vol. 30, no. 4, pp. 920–926, Jul./Aug. 1994.
- [2] J.-M. Kim and S.-K. Sul, "Speed control of interior permanent magnet synchronous motor drive for the flux weakening operation," *IEEE Trans. Ind. Appl.*, vol. 33, no. 1, pp. 43–48, Jan./Feb. 1997.
- [3] H. Kim, M. W. Degner, J. M. Guerrero, F. Briz, and R. D. Lorenz, "Discrete-time current regulator design for AC machine drives," *IEEE Trans. Ind. Appl.*, vol. 46, no. 4, pp. 1425–1435, Jul./Aug. 2010.
- [4] K. D. Hoang and H. K. A. Aorith, "Online control of IPMSM drives for traction applications considering machine parameter and inverter nonlinearities," *IEEE Trans. Transport. Electrification*, vol. 1, no. 4, pp. 312–325, Dec. 2015.
- [5] H. A. A. Awan, S. E. Saarakkala, and M. Hinkkanen, "Flux-linkage-based current control of saturated synchronous motors," *IEEE Trans. Ind. Appl.*, vol. 55, no. 5, pp. 4762–4769, Sep./Oct. 2019.
- [6] S.-W. Su, H. Börngen, C. M. Hackl, and R. Kennel, "Nonlinear current control of reluctance synchronous machines with analytical flux linkage

- prototype functions,” *IEEE Open J. Ind. Electron.*, vol. 3, pp. 582–593, 2022.
- [7] H. Hofmann, S. Sanders, and A. EL-Antably, “Stator-flux-oriented vector control of synchronous reluctance machines with maximized efficiency,” *IEEE Trans. Ind. Electron.*, vol. 51, no. 5, pp. 1066–1072, Oct. 2004.
- [8] G. Pellegrino, E. Armando, and P. Guglielmi, “Direct flux field-oriented control of IPM drives with variable DC link in the field-weakening region,” *IEEE Trans. Ind. Appl.*, vol. 45, no. 5, pp. 1619–1627, Sep./Oct. 2009.
- [9] Y. Inoue, S. Morimoto, and M. Sanada, “Comparative study of PMSM drive systems based on current control and direct torque control in flux-weakening control region,” *IEEE Trans. Ind. Appl.*, vol. 48, no. 6, pp. 2382–2389, Nov./Dec. 2012.
- [10] B. Boazzo and G. Pellegrino, “Model-based direct flux vector control of permanent-magnet synchronous motor drives,” *IEEE Trans. Ind. Appl.*, vol. 51, no. 4, pp. 3126–3136, July–Aug. 2015.
- [11] A. Yousefi-Talouki, P. Pescetto, and G. Pellegrino, “Sensorless direct flux vector control of synchronous reluctance motors including standstill, MTPA, and flux weakening,” *IEEE Trans. Ind. Appl.*, vol. 53, no. 4, pp. 3598–3608, Jul./Aug. 2017.
- [12] S. Rubino, L. Tolosano, F. Mandrile, E. Armando, and R. Bojoi, “Flux polar control (FPC): A unified torque controller for AC motor drives,” *IEEE Trans. Ind. Appl.*, vol. 59, no. 4, pp. 4140–4163, Jul./Aug. 2023.
- [13] I. Takahashi and T. Noguchi, “A new quick-response and high-efficiency control strategy of an induction motor,” *IEEE Trans. Ind. Appl.*, vol. IA-22, no. 5, pp. 820–827, Sep./Oct. 1986.
- [14] A. Tripathi, A. Khambadkone, and S. Panda, “Torque ripple analysis and dynamic performance of a space vector modulation based control method for AC-drives,” *IEEE Trans. Power Electron.*, vol. 20, no. 2, pp. 485–492, Mar. 2005.
- [15] J. S. Lee, C.-H. Choi, J.-K. Seok, and R. D. Lorenz, “Deadbeat-direct torque and flux control of interior permanent magnet synchronous machines with discrete time stator current and stator flux linkage observer,” *IEEE Trans. Ind. Appl.*, vol. 47, no. 4, pp. 1749–1758, Jul./Aug. 2011.
- [16] H. A. A. Awan, M. Hinkkanen, R. Bojoi, and G. Pellegrino, “Stator-flux-oriented control of synchronous motors: A systematic design procedure,” *IEEE Trans. Ind. Appl.*, vol. 55, no. 5, pp. 4811–4820, Jul./Aug. 2019.
- [17] A. Isidori, *Nonlinear Control Systems*, 3rd ed. London, U.K.: Springer, 1995.
- [18] A. Varatharajan, G. Pellegrino, and E. Armando, “Direct flux vector control of synchronous motor drives: Accurate decoupled control with online adaptive maximum torque per ampere and maximum torque per volts evaluation,” *IEEE Trans. Ind. Electron.*, vol. 69, no. 2, pp. 1235–1243, Feb. 2022.
- [19] P. D. C. Perera, F. Blaabjerg, J. K. Pedersen, and P. Thøgersen, “A sensorless, stable V/f control method for permanent-magnet synchronous motor drives,” *IEEE Trans. Ind. Appl.*, vol. 39, no. 3, pp. 783–791, May/Jun. 2003.
- [20] Z. Tang, X. Li, S. Dusmez, and B. Akin, “A new V/f-based sensorless MTPA control for IPMSM drives,” *IEEE Trans. Power Electron.*, vol. 31, no. 6, pp. 4400–4415, Jun. 2016.
- [21] K. Lee and Y. Han, “MTPA control strategy based on signal injection for V/f scalar-controlled surface permanent magnet synchronous machine drives,” *IEEE Access*, vol. 8, pp. 96036–96044, 2020.
- [22] L. Tiitinen, M. Hinkkanen, J. Kukkola, M. Routimo, G. Pellegrino, and L. Harnefors, “Stable and passive observer-based V/Hz control for synchronous motors,” in *Proc. IEEE Energy Convers. Congress Expo.*, Detroit, MI, Oct. 2022, pp. 1–8.
- [23] H. K. Khalil, *Nonlinear Systems*, 2nd ed. Upper Saddle River, NJ, USA: Prentice-Hall, 1996.
- [24] M. Hinkkanen, S. E. Saarakkala, H. A. A. Awan, E. Mölsä, and T. Tuovinen, “Observers for sensorless synchronous motor drives: Framework for design and analysis,” *IEEE Trans. Ind. Appl.*, vol. 54, no. 6, pp. 6090–6100, Nov./Dec. 2018.
- [25] T. Tuovinen, H. A. A. Awan, J. Kukkola, S. E. Saarakkala, and M. Hinkkanen, “Permanent-magnet flux adaptation for sensorless synchronous motor drives,” in *Proc. IEEE 9th Int. Symp. Sensorless Control Electr. Drives (SLED)*, Helsinki, Finland, Sep. 2018, pp. 138–143.
- [26] M. Zhang, B. Xia, and J. Zhang, “Parameter design and convergence analysis of flux observer for sensorless PMSM drives,” *IEEE Trans. Energy Convers.*, vol. 37, no. 4, pp. 2512–2524, Dec. 2022.
- [27] M. Sassano and A. Astolfi, “A local separation principle via dynamic approximate feedback and observer linearization for a class of nonlinear systems,” *IEEE Trans. Autom. Control*, vol. 64, no. 1, pp. 111–126, Jan. 2019.
- [28] T. Tuovinen and M. Hinkkanen, “Adaptive full-order observer with high-frequency signal injection for synchronous reluctance motor drives,” *IEEE Trans. Emerg. Sel. Topics Power Electron.*, vol. 2, no. 2, pp. 181–189, Jun. 2014.
- [29] A. Yousefi-Talouki, P. Pescetto, G. Pellegrino, and I. Boldea, “Combined active flux and high-frequency injection methods for sensorless direct-flux vector control of synchronous reluctance machines,” *IEEE Trans. Power Electron.*, vol. 33, no. 3, pp. 2447–2457, Mar. 2018.
- [30] H. Hartikainen, L. Tiitinen, S. Laine, and M. Hinkkanen, “Identification of mechanical impedance of an electric machine drive for drivetrain design,” in *Proc. IEEE Int. Electr. Mach. Drives Conf.*, San Francisco, CA, May 2023, pp. 1–6.
- [31] Z. Qu, T. Tuovinen, and M. Hinkkanen, “Inclusion of magnetic saturation in dynamic models of synchronous reluctance motors,” in *Proc. Int. Conf. Electr. Mach.*, Sep. 2012, pp. 994–1000.
- [32] M. Hinkkanen, P. Pescetto, E. Mölsä, S. E. Saarakkala, G. Pellegrino, and R. Bojoi, “Sensorless self-commissioning of synchronous reluctance motors at standstill without rotor locking,” *IEEE Trans. Ind. Appl.*, vol. 53, no. 3, pp. 2120–2129, May/Jun. 2017.
- [33] H. A. A. Awan, Z. Song, S. E. Saarakkala, and M. Hinkkanen, “Optimal torque control of saturated synchronous motors: Plug-and-play method,” *IEEE Trans. Ind. Appl.*, vol. 54, no. 6, pp. 6110–6120, Nov./Dec. 2018.
- [34] N. Monzen, F. Stroebel, H. Palm, and C. M. Hackl, “Multiobjective hyperparameter optimization of artificial neural networks for optimal feedforward torque control of synchronous machines,” *IEEE Open J. Ind. Electron.*, vol. 5, pp. 41–53, 2024.
- [35] W. Peters, O. Wallscheid, and J. Böcker, “A precise open-loop torque control for an interior permanent magnet synchronous motor (IPMSM) considering iron losses,” in *Proc. Annu. Conf. IEEE Ind. Electron. Soc.*, Oct. 2012, pp. 2877–2882.
- [36] A. Varatharajan, G. Pellegrino, and E. Armando, “Direct flux vector control of synchronous motor drives: A small-signal model for optimal reference generation,” *IEEE Trans. Power Electron.*, vol. 36, no. 9, pp. 10526–10535, Sep. 2021.



Lauri Tiitinen received the B.Sc.(Tech.) and M.Sc.(Tech.) degrees in electrical engineering in 2019 and 2020, respectively, from Aalto University, Espoo, Finland, where he is currently working toward the D.Sc.(Tech.) degree in electrical engineering.

His research interests include control and self-commissioning of electric motor drives.

Mr. Tiitinen was the recipient of the Second Prize Paper Awards in 2023 International Symposium on Sensorless Control for Electric Drives

(SLED) and the 2018 IEEE Industry Applications Society Industrial Drives Committee.



Marko Hinkkanen (Fellow, IEEE) received the M.Sc.(Eng.) and D.Sc.(Tech.) degrees in electrical engineering from the Helsinki University of Technology, Espoo, Finland, in 2000 and 2004, respectively.

He is currently a Full Professor with the School of Electrical Engineering, Aalto University, Espoo. His research interests include control systems, electric machine drives, and power converters.

Dr. Hinkkanen was the recipient of eight paper awards, including the 2016 International Conference on Electrical Machines (ICEM) Brian J. Chalmers Best Paper Award, and the 2016 and 2018 IEEE Industry Applications Society Industrial Drives Committee Best Paper Awards. He was the co-recipient of the 2020 SEMIKRON Innovation Award. He was the General Co-Chair of the 2018 IEEE 9th International Symposium on Sensorless Control for Electric Drives (SLED). He is an Associate Editor of IEEE TRANSACTIONS ON ENERGY CONVERSION and *IET Electric Power Applications*.



time Visiting Professor in electrical drives with Chalmers University of

Lennart Harnefors (Fellow, IEEE) received the M.Sc., Licentiate, and Ph.D. degrees in electrical engineering from Royal Institute of Technology (KTH), Stockholm, Sweden, in 1993, 1995, and 1997, respectively, and the Docent (D.Sc.) degree in industrial automation from Lund University, Lund, Sweden, in 2000.

From 1994 to 2005, he was with Mälardalen University, Västerås, Sweden, where he has been a Professor in electrical engineering, since 2001. From 2001 to 2005, he was a part-

time Visiting Professor with Aalto University, Espoo, Finland. His research interests include control and dynamic analysis of power electronic systems, particularly grid-connected converters and ac drives.

Dr. Harnefors is an Editor for IEEE JOURNAL OF EMERGING AND SELECTED TOPICS IN POWER ELECTRONICS. He was the recipient of the 2020 IEEE Modeling and Control Technical Achievement Award.